

# Fluid simulation of dispersive and nondispersive ion acoustic waves in the presence of superthermal electrons

Ajay Lotekar,<sup>a)</sup> Amar Kakad,<sup>b)</sup> and Bharati Kakad<sup>c)</sup>

Indian Institute of Geomagnetism, New Panvel, Navi Mumbai 410-218, India

(Received 20 August 2016; accepted 21 September 2016; published online 13 October 2016)

One-dimensional fluid simulation is performed for the unmagnetized plasma consisting of cold fluid ions and superthermal electrons. Such a plasma system supports the generation of ion acoustic (IA) waves. A standard Gaussian type perturbation is used in both electron and ion equilibrium densities to excite the IA waves. The evolutionary profiles of the IA waves are obtained by varying the superthermal index and the amplitude of the initial perturbation. This simulation demonstrates that the amplitude of the initial perturbation and the superthermal index play an important role in determining the time evolution and the characteristics of the generated IA waves. The initial density perturbation in the system creates charge separation that drives the finite electrostatic potential in the system. This electrostatic potential later evolves into the dispersive and nondispersive IA waves in the simulation system. The density perturbation with the amplitude smaller than 10% of the equilibrium plasma density evolves into the dispersive IA waves, whereas larger density perturbations evolve into both dispersive and nondispersive IA waves for lower and higher superthermal index. The dispersive IA waves are the IA oscillations that propagate with constant ion plasma frequency, whereas the nondispersive IA waves are the IA solitary pulses (termed as IA solitons in the stability region) that propagate with the constant wave speed. The characteristics of the stable nondispersive IA solitons are found to be consistent with the nonlinear fluid theory. To the best of our knowledge, this is the first fluid simulation study that has considered the superthermal distributions for the plasma species to model the electrostatic solitary waves. Published by AIP Publishing. [<http://dx.doi.org/10.1063/1.4964478>]

## I. INTRODUCTION

Electrostatic solitary waves (ESWs) is a topic of considerable interest in space<sup>1–3</sup> and laboratory<sup>4,5</sup> plasma physics. The ESWs contribute to the broadband electrostatic noise, which is observed in different regions of the Earth's magnetosphere.<sup>6,7</sup> These waves are also linked with the interplanetary shocks,<sup>1</sup> magnetic reconnection,<sup>3</sup> and particle acceleration<sup>2,8</sup> processes in space plasma.

Numerous works have been done to model ESWs with the electron and ion acoustic (IA) soliton models, which are based on the multi-fluid approach. In these fluid models, the reductive perturbation and the Sagdeev's pseudopotential methods are used to model the ESWs. The reductive perturbation technique is used to study the small amplitude ion/electron acoustic solitons in which the Korteweg-de Vries (KdV) equation is solved in the model.<sup>9–13</sup> The arbitrary amplitude ion/electron acoustic solitons are studied by the Sagdeev's pseudopotential method, in which the stationary solution from the fluid equations is derived, and the Mach number range is obtained for existence of the solitons.<sup>14–20</sup> Most of these models are studied for the plasma having thermal distribution, i.e., Maxwellian distribution. However, satellite observations suggest that the particles often follow non-Maxwellian (superthermal) type velocity distribution,

where the tail of the distribution function decreases as a power law of the velocity. This type of distribution occurs due to the population of the superthermal particles with the velocity greater than the average thermal velocity of the particles.

Spacecraft observations have confirmed the presence of superthermal particle distribution in near Earth's plasma environment (e.g., Earth's plasma sheet region,<sup>21–23</sup> Earth's magnetosheath region,<sup>24</sup> Earth's radiation belt region,<sup>25,26</sup> and in solar wind<sup>27,28</sup>) and in laboratory<sup>29,30</sup> plasma. Such distributions are well fitted by the so called kappa distribution function.<sup>29,30</sup> Olbert,<sup>31</sup> in 1968, first used the empirical form of the kappa velocity distribution function to describe free electron distribution in the satellite frame,<sup>31</sup> followed by Vasyliunas<sup>32</sup> who used three-dimensional isotropic kappa velocity distribution function to explain the low-energy electron population in the Earth's magnetosphere.<sup>32</sup> The three-dimensional isotropic kappa velocity distribution function has the following form:<sup>32,33</sup>

$$f_{\kappa}(v_s) = \frac{n_{0s}}{(\pi\kappa\theta_s^2)^{3/2}} \frac{\Gamma(\kappa+1)}{\Gamma(\kappa-1/2)} \left[1 + \frac{v_s^2}{\kappa\theta_s^2}\right]^{-(\kappa+1)}. \quad (1)$$

In the equation above,  $\Gamma$  is the gamma function, and  $n_{0s}$  and  $v_s$  are, respectively, the density and velocity of plasma species  $s$ .  $\theta_s^2 = [(\kappa - 3/2)/\kappa]v_{th,s}^2$  is the most probable speed or characteristic speed, where  $v_{th,s} = (2k_B T_s/m_s)^{1/2}$  is the

<sup>a)</sup>ablotekar@gmail.com

<sup>b)</sup>amar@iigs.iigm.res.in

<sup>c)</sup>ebharati@iigs.iigm.res.in

thermal speed of the plasma species,  $k_B$  is the Boltzmann constant.  $T_s$  and  $m_s$  are temperature and mass of the plasma species. The spectral index  $\kappa$  decides the slope of the tail of the distribution function, and it is always greater than 0.5. The smaller value of  $\kappa$  enhances the superthermal population in the system, which leads to decrease in the slope of the tail. As the kappa index  $\kappa \rightarrow \infty$ , the kappa distribution function converges to Maxwellian distribution function. For space plasma, the kappa index is observed in the range,<sup>34</sup>  $2 < \kappa < 6$ . The one-dimensional form of the kappa distribution function can be obtained by integrating Equation (1) over two velocity space coordinates as<sup>33</sup>

$$f_\kappa(v_s) = \frac{n_{0s}}{(\pi\kappa\theta_s^2)^{1/2}} \frac{\Gamma(\kappa)}{\Gamma(\kappa - 1/2)} \left[ 1 + \frac{v_s^2}{\kappa\theta_s^2} \right]^{-\kappa}. \quad (2)$$

The presence of superthermal particles in space and laboratory plasma suggests their role in the existence of ESWs, which is confirmed by different theoretical models.<sup>35–37</sup> In this context, recently, there has been many theoretical studies carried out for understanding the effect of superthermal particles on the existence conditions and the characteristics of the ion acoustic solitary waves (IASWs) for different plasma compositions.<sup>35–40</sup> However, the conclusions drawn in these studies are based on the theoretical analysis of different plasma models using either reductive perturbation or the Sagdeev's pseudopotential techniques. These approaches provide the existing domain of stationary solitary wave solution that gives ESW profile for the given set of parameters. However, these methods are not capable of giving the evolutionary information of the ESWs. Moreover, various assumptions considered in these models to get an analytical solution suppress the nonlinear effects in the system. To overcome such problems, a numerical simulation technique can be a good supplementary tool, which can be used to get evolutionary information of the ESWs. Recently, Kakad *et al.*<sup>41–43</sup> used fluid simulation to study the characteristics of IASWs in electron-ion plasma by treating these species as fluid. They have successfully validated the Sagdeev's pseudopotential technique, which has been used in modeling the ESWs from past few decades.

In this study, we focus on the consequence of the superthermal electron population on the evolution of IASWs. Considering the ambiguity of the kappa distribution and its involvement in the formation of the ESWs, the numerical simulation of the model would be the suitable approach for the study. Hence, we have developed one-dimensional fluid code for the unmagnetized collisionless plasma, which consists of cold fluid ions and the superthermal electrons. To the best of our knowledge, this is the first fluid simulation study where the superthermal distribution is considered in modeling the ESWs. In Section II, we discuss the plasma model along with the numerical methods used in the simulation. The simulation results are explained in Section III. We validate the theoretical results by comparing them with the simulation in Section IV. Finally, we conclude the results in Section V.

## II. SIMULATION MODEL

We consider homogeneous two-component unmagnetized plasma, which consists of cold ions (charge  $q_i = e$ , mass  $m_i$ ) and hot electrons (charge  $q_e = -e$ , mass  $m_e$ ) in the one-dimensional system. The ions are governed by the fluid equations of continuity and momentum

$$\frac{\partial n_i}{\partial t} + \frac{\partial(n_i v_i)}{\partial x} = 0, \quad (3)$$

$$\frac{\partial v_i}{\partial t} + v_i \frac{\partial v_i}{\partial x} = -\frac{q_i}{m_i} \frac{\partial \phi}{\partial x}, \quad (4)$$

where  $n_i$  and  $v_i$  are density and velocity of the ions in the  $x$ -direction, respectively,  $\phi$  is the electrostatic potential in the system. In the model, electrons are assumed as superthermal particles regulated by the kappa distribution function given by Equation (2). The electron density can be obtained by taking the first moment of the one-dimensional kappa velocity distribution function as,

$$n_e = n_{e0} \left[ 1 - \frac{e\phi}{(\kappa - 3/2)k_B T_e} \right]^{-\kappa+1/2}. \quad (5)$$

In the equation above,  $T_e$  is the temperature of the electrons. The electron and ion fluids are coupled by Poisson equation

$$\frac{\partial^2 \phi}{\partial x^2} = -(q_i n_i + q_e n_e) / \epsilon_0. \quad (6)$$

At the equilibrium state, plasma follows quasi-neutrality, under which the ion density is equivalent to the electron density, i.e.,  $n_{i0} = n_{e0}$ . Here  $n_{i0}$  and  $n_{e0}$  are ion and electron density at the equilibrium, respectively. For simplicity, we normalized Equations (3)–(6) with appropriate scaling quantities. So Equations (3), (4), and (6) can be written as

$$\frac{\partial N_i}{\partial t_n} + \frac{\partial(N_i U_i)}{\partial x_n} = 0, \quad (7)$$

$$\frac{\partial U_i}{\partial t_n} + U_i \frac{\partial U_i}{\partial x_n} = -\frac{\partial \Phi}{\partial x_n}, \quad (8)$$

$$\frac{\partial^2 \Phi}{\partial x_n^2} = -N_i + \left( 1 - \frac{\Phi}{\kappa - 3/2} \right)^{-\kappa+1/2}. \quad (9)$$

In the equation above, the ion fluid velocity  $v_i$ , the ion density  $n_i$ , and the electrostatic potential  $\phi$  are normalized as  $U_i = v_i / C_{IA}$ ,  $N_i = n_i / n_{i0}$ , and  $\Phi = e\phi / k_B T_e$ , respectively. The space and time are normalized by the electron Debye length  $\lambda_{De} = (k_B T_e \epsilon_0 / n_{e0} e^2)^{1/2}$  and inverse of the ion plasma oscillation frequency  $\omega_{pi}^{-1} = (\epsilon_0 m_i / n_{i0} e^2)^{1/2}$ , respectively. It gives  $x_n = x / \lambda_{De}$  and  $t_n = \omega_{pi} t$ . The characteristic ion acoustic sound speed used in the velocity normalization is  $C_{IA} = (k_B T_e / m_i)^{1/2}$ .

For the numerical solution of the set of Equations (7)–(9) the system is fragmented into the equidistance grid points in space and time. All the plasma quantities are calculated on the grid points. In this discretized system, the first order differential operator is replaced by its corresponding difference formula. The spatial derivatives in Equations (7)

and (8) are replaced by the central finite difference formula<sup>41,44,45</sup>

$$\frac{\partial F_h}{\partial x} = \frac{8(F_{h+1} - F_{h-1}) - F_{h+2} + F_{h-2}}{12\Delta x} + O(\Delta x^4). \quad (10)$$

Here,  $F_h$  can be any quantity where spatial derivative intends to find at  $h$ -space grid point. The accuracy of this method is up to the fourth order of grid size ( $\Delta x$ ). The time integration of Equations (7) and (8) are done by using leap-frog method,<sup>45</sup> which is second order accurate in time. To remove the high-frequency errors introduced due to the spatial discretization, we use the compensating filter<sup>45</sup>

$$F_h^* = \frac{5}{8}F_h + \frac{1}{4}(F_{h-1} + F_{h+1}) - \frac{1}{16}(F_{h-2} + F_{h+2}). \quad (11)$$

In the equation above,  $F_h^*$  is the filtered quantity at  $h$  grid point. We have performed simulation for the one-dimensional system with periodic boundary conditions. For all simulation runs, the ion velocity at  $t=0$  is zero, i.e.,  $v_i(x) = 0$ . In addition, there is no electric field initially present in the system, which gives  $\phi = 0$  at  $t=0$ . The background electron and ion densities are set as  $n_{i0} = n_{e0} = n_0 = 1$ . The background equilibrium densities of the species are superimposed by Gaussian type perturbation

$$\delta n = \Delta n \exp\left[-\left(\frac{x-x_c}{l_0}\right)^2\right]. \quad (12)$$

In the equation above,  $\Delta n$  is the amplitude of the perturbation,  $x$  is the position on  $x$ -axis,  $x_c$  is the center of the system, and  $l_0$  controls width of the perturbation. Hence, the form of the perturbed density at the equilibrium is  $n_s = n_{s0} + \delta n$ , with making the substitution from Equation (12) it reads as

$$n_s = n_{s0} + \Delta n \exp\left[-\left(\frac{x-x_c}{l_0}\right)^2\right]. \quad (13)$$

Here  $s = e, i$  for electrons and ions, respectively. All simulation runs are performed for the grid spacing  $\Delta x = 0.2\lambda_{De}$ , time interval  $\omega_{pi}\Delta t = 0.1$ , and width of the perturbation  $l_0 = 2\lambda_{De}$ . The system length,  $Lx$ , is varied as per the requirement of the propagation of IASWs to achieve stability before reaching at the boundaries of the system. The details of the input parameters of all the simulation runs are given in Table I.

In this model, the electrons do not have any time dependent equation to update its density value to the next time step. The electrostatic potential dependency of the electron density makes Poisson equation numerically unstable with an implication of the conventional method for the solution. Hence, we use the iterative approach with successive-over-relaxation (SOR) method proposed by Lotekar *et al.*<sup>46</sup> for such kind of Poisson equation. In this approach, the approximate value of potential can be obtained by giving an initial guess, suitable relaxation parameter ( $\zeta$ ), and tolerance ( $\tau$ ) so that the simulation code runs numerically stable. In this simulation, we have taken  $\zeta = 1.7$  and  $\tau = 10^{-10}$  for all the simulation runs.

TABLE I. Table contains the input parameter information of 56 Runs given for the different combination of  $\kappa$  and  $\Delta n$ . The information of the specific simulation run reads as, e.g., Run-1(I) has input parameters  $\kappa = 2$ ,  $\Delta n = 5\%$ ,  $L = 50,000$ ,  $l_0 = 2$ ,  $\Delta x = 0.2$ , and  $\Delta t = 0.1$ . For Run-1(II), only the  $\kappa$  value will be changed, i.e.,  $\kappa = 4$  in this case and the other parameters will be same as Run-1(I).

Run	$\kappa$							$\Delta n$	L [ $\lambda_{De}$ ]	$l_0$	$\Delta x[\lambda_{De}]$	$\Delta t[\omega_{pi}^{-1}]$
	Sub run number											
1								0.05	50 000	2	0.2	0.1
2								0.1				
3								0.15				
4	2	4	6	8	10	15	20	0.2				
5	I	II	III	IV	V	VI	VII	0.35	30 000			
6								0.5	20 000			
7								0.75				
8								1				

### III. SIMULATION RESULTS

We have used a total of 56 simulation runs for the different combination of the values of  $\kappa$  and  $\Delta n$ . The value of  $\kappa$  index varies as  $\kappa = 2, 4, 6, 8, 10$ , and  $20$ . For the fixed value of the  $\kappa$  index, the amplitude of initial density perturbation (IDP) varies from  $\Delta n = 0.05 - 1$  (i.e., 5%–100% of the equilibrium density). These combinations of the  $\kappa$  and  $\Delta n$  are given in Table I. For the appropriate values of the IDP, it is found that the perturbation evolved into two IASW pulses and two wave packets of IA oscillations. The IASW pulses become significantly stable after some time of their formation, where they are referred as IA solitons and the region is called as the stability region. The evolutionary process of these structures in different simulation runs is discussed in Subsec. III A.

#### A. Generation and evolution of IA waves

Figure 1 shows the schematic of the formation and the evolution of the IA solitons, when the short wavelength IDP

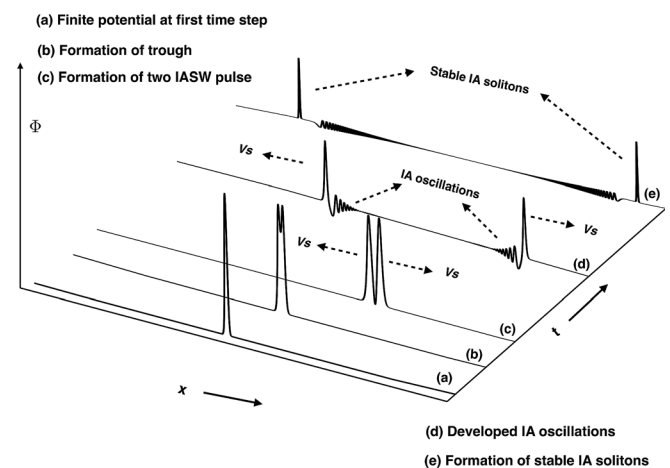


FIG. 1. Schematic diagram shows the evolution of the ion acoustic solitons and ion acoustic oscillations in the system. (a) Finite potential pulse formation at first time step. (b) Formation of two IA solitary pulses and their propagation toward the left and right boundaries of the simulation. (c) Generation of IA oscillations at the trailing edge of both pulses. (d) Formation of two IA solitons and the IA oscillations.

is superimposed on the background electron and ion densities. The short wavelength perturbations considered here are same as described in Kakad *et al.*<sup>41</sup> The quasi-neutrality at the equilibrium causes the electrostatic potential in the system to be zero. As electrons follows the kappa distribution, it leads to the generation of the finite electrostatic potential at the next time step in the simulation system. In Figure 1(a), the pulse shown is the finite electrostatic potential at the first time step in the system. It is observed that the amplitude of the electrostatic potential in the system reduced with time. This decrease of the potential eventually stops after some time and the pulse starts splitting from its top point through formation of the trough as shown in Figure 1(b). Once the value of the  $\Phi$  approaches to zero at the centre of the trough, two identical solitary pulses are formed in the system as seen in Figure 1(c). Further these two pulses propagate with the speed  $V_s$  in a direction opposite to each other, i.e., towards the boundaries of the simulation system as shown in Figure 1(d). These pulses are identified as IASW pulses. In the propagation, the amplitude of these IASW pulses slowly decreases, and some oscillations are generated at the trailing edge of both pulses. These oscillations are identified as IA oscillations. The amplitude of the IA oscillations is considerably smaller than the amplitude of the IA solitary pulse. The IA oscillations along with the IASW pulses are shown in Figure 1(d). The IA oscillations propagate with the speed,  $V_{s0}$  such that the IA oscillations lag behind the IASW pulses (i.e.,  $V_{s0} < V_s$ ). Later, after sufficient time, the IA oscillations get detached from IASW pulses and these pulses become adequately stable. During this stage, both IASW

pulses propagate with nearly constant amplitude, width, and speed. These stable structures are shown in Figure 1(e) and are termed as IA solitons. From the overall 56 simulation runs of different  $\kappa$  and  $\Delta n$ , we find that the superthermal population and the amplitude of the IDP govern the evolutionary characteristics of the IASWs and the IA oscillations, which is discussed in Subsecs. III B–III D.

## B. Spatio-temporal variation of the IA waves

To study the effect of the superthermal population on the formation and evolution of the IA oscillations and IASWs, we investigate the spatio-temporal variation of the electrostatic potential  $\Phi$  in the system. Figure 2 shows four panels of the evolution of  $\Phi$  in space and time for kappa index  $\kappa=2$  and 20 with the low ( $\Delta n=0.05$ ) and high ( $\Delta n=0.5$ ) amplitudes of IDP. The low (high) value of the kappa corresponds to the higher (lower) population of the superthermal electrons. The simulation system length for the run with  $\Delta n=0.05$  is  $50000\lambda_{De}$ , and that for the  $\Delta n=0.5$  it is  $20000\lambda_{De}$ . In Figure 2, we show only part of the simulation system, i.e., from  $Lx - x_c = -6000$  to  $6000\lambda_{De}$  for all the runs. In all the plots,  $x - x_c = 0$  represents the center of the simulation system at which the IDP is introduced at  $\omega_{pi}t = 0$ . Figure 2 shows the spatio-temporal variation of  $\Phi$  in the simulation for (a) Run-1(I):  $\Delta n = 0.05$ ,  $\kappa = 2$ , (b) Run-1(VII):  $\Delta n = 0.05$ ,  $\kappa = 20$ , (c) Run-6(I):  $\Delta n = 0.5$ ,  $\kappa = 2$ , and (d) Run-6(VII):  $\Delta n = 0.5$ ,  $\kappa = 20$ .

In general, all four panels of Figure 2 show two identical sets of band structures that represent the IASW pulses and

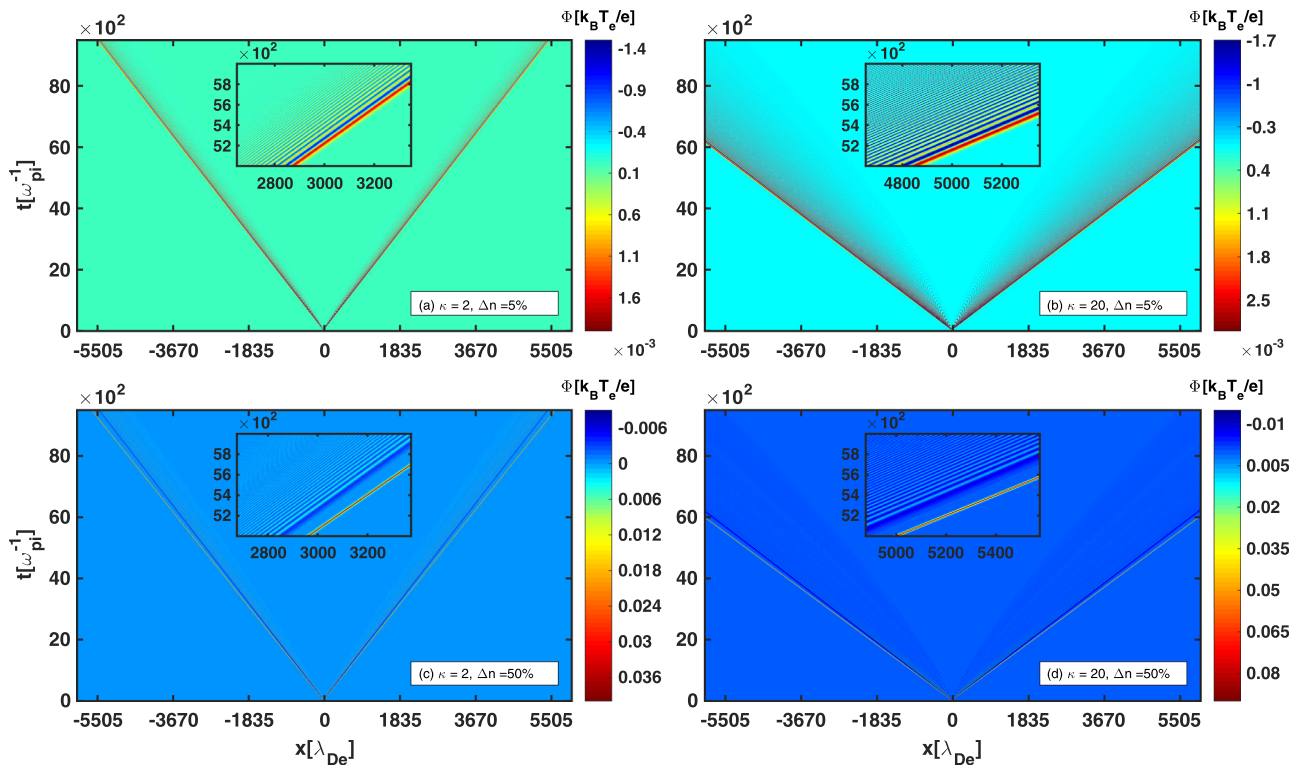


FIG. 2. Spatiotemporal evolution of the electrostatic potential in the system for different combination of  $\kappa$  and  $\Delta n$ : (a) Run-1(I), (b) Run-1(VII), (c) Run-6(I), and (d) Run-6(VII). In all the four plots, intense red band is due to the IASW pulse and the other alternate blue and light red color bands are due to the IA oscillations.

the IA oscillations propagating along both the positive and negative  $x$ -directions. The small window at the center of the respective plots shows the magnified image, where some region of the IA waves propagating in the positive  $x$ -direction is illustrated. The IASW pulses in the system are associated with positive potential and its amplitude is higher as compared with that of IA oscillations, which possess both positive and negative potentials. Therefore, the dark red bands in all four panels of Figure 2 represent the IASW pulse, whereas the alternate blue color bands represent the IA oscillations. The inverse of the slope of the red bands in each panel of this figure gives the speed of the IA solitary pulse in the corresponding run. The positive (negative) value of the inverse of slope indicates the IA pulse propagating in the positive (negative)  $x$ -direction. From this figure, it is clear that in each simulation run, there are two sets of the IA solitary pulse and IA oscillations that are propagating opposite to each other in the system.

The difference in the spatio-temporal characteristics of the electrostatic potential at the same time interval is clearly seen in Figure 2 for the different perturbations. Comparison of Figure 2(a) with 2(c), and Figure 2(b) with 2(d), yields that the increase in the amplitude of IDP results in the higher amplitudes of both IASW pulse and IA oscillations. It is noticed that the spread in the IA oscillations is increased for the higher amplitude IDPs and larger superthermal index  $\kappa$ , which indicates the wider spatial extent of these IA oscillations. Hence, more number of alternate blue colour bands are visible in the lower panels of Figure 2 as compared with the upper panels. The other interesting feature is the bands associated with the IA pulse and the IA oscillations are found to be well separated for higher amplitude IDPs. For example, in Figures 2(a) and 2(b), where  $\Delta n = 0.05$ , it is observed that the IASW pulses and IA oscillations did not detach from each other even after a very long time during the course of evolution. This indicates that the IASW pulses and the oscillations propagate at almost comparable speed.

It is also observed that the speeds and amplitudes of IASW pulses and oscillations in case of lower value of the kappa are smaller as compared with higher  $\kappa$ , while the same IDP is used to perturb the system. This is because the lower (higher) kappa index corresponds to the presence of considerably higher (lower) superthermal population. This indicates that the system with more number of superthermal electrons has smaller most probable thermal speed. Generally, the most probable thermal speed of the particles decides the amplitudes and speeds of different wave modes in the system. Therefore, for the system with the superthermal electrons (i.e., lower  $\kappa$ ) the wave speed is found to be smaller as compared with the wave speeds in the Maxwellian system (higher  $\kappa$ ).

### C. Dispersive and nondispersive IA waves

It is known that the waves that exist in the plasma are nonlinearly coupled. The free energy given initially in the form of IDP to the system is transferred to the different wave modes. In such case, the dispersion characteristics of the evolving plasma system will help to identify the different wave modes supported by the plasma. We have obtained the

power spectrum from the Fourier transformation of the electrostatic potential over space and time. Figure 3 shows the power spectra of the four different simulation runs that are depicted in Figure 2. These power spectra are taken over the period of  $\omega_{pi}t = 0 - 200$ . In all four plots, gray and white dashed curves are plotted from the linear dispersion relations derived from Equations (7)–(9). Among these lines, the white dashed lines are plotted from the linear dispersion equation that is obtained without considering the plasma approximation of the quasi-neutrality, i.e.,  $N_i \neq N_e$ , which is given as

$$\omega^2 = \frac{k^2}{k^2 + (\kappa - 1/2)/(\kappa - 3/2)}, \quad (14)$$

where  $\omega$  is the frequency and  $k$  is the wave number. The dashed gray line is from the linear dispersion equation with the consideration of the plasma approximation ( $N_i = N_e$ ) and it reads as

$$\omega^2 = \frac{k^2}{(\kappa - 1/2)/(\kappa - 3/2)}. \quad (15)$$

Figure 3(a) shows the power spectra of the electrostatic potential taken for the simulation Run-1(I),  $\Delta n = 0.05$  and  $\kappa = 2$ . This plot shows the strong dispersion curves that follow the white dashed line and the weak dispersion curves that follow the gray lines. The strong dispersion curves are diagnosed as the IA oscillations, which propagate with the constant frequency. The gray line indicates the constant velocity wave mode that appears as nondispersive IASW pulses. This shows that the energy given to the system in terms of the IDP is mainly transferred to the dispersive IA oscillations mode in the system. Figure 3(b) also shows similar mode characteristics for the simulation Run-1(VII),  $\Delta n = 0.05$  and  $\kappa = 20$ . The major difference between these two cases is that the dispersion curve associated with the dispersive mode in Fig. 3(b) has more power than that in Figure 3(a). Second, the speed of the IA oscillations in the case of Fig. 3(b) is higher than that in Fig. 3(a).

The dispersion plot shown in Figure 3(c) for the Run-6(I) ( $\Delta n = 0.5$ ,  $\kappa = 2$ ) and in Figure 3(d) for the Run-6(VII) ( $\Delta n = 0.5$ ,  $\kappa = 20$ ) are the cases of the higher amplitude IDPs. In these figures, two types of dispersion curves are clearly visible. It is found that the one dispersion curve follows the white line while another follows the dashed gray line. The dispersion which follows the dashed gray line is diagnosed as nondispersive IASW pulses, which propagate with constant wave speed. The other dispersion follows the dashed white line, which is identified as the dispersive IA oscillations. From the dispersion plots of these four simulation runs, it is observed that the increase in the  $\kappa$  index and IDP amplitude results in the higher speed of the dispersive and nondispersive IA wave modes. These observations are consistent with the observations from the spatio-temporal evolution plots shown in Figure 2.

### D. Kinetic and potential energies during evolution of the IA waves

Figure 4 shows the evolution of the average kinetic  $\langle KE \rangle$  and potential energies  $\langle U \rangle$  of the system during

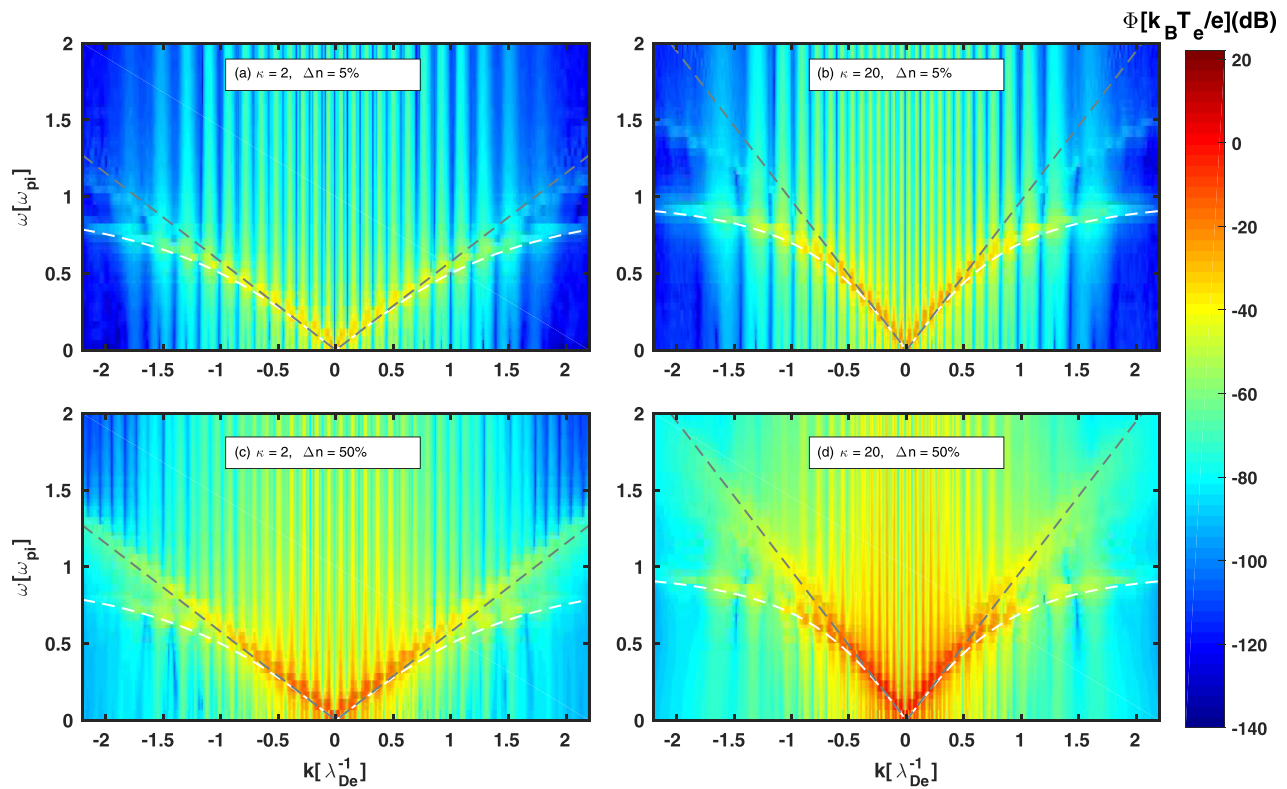


FIG. 3.  $\omega$ - $k$  diagram during  $\omega_{pi}t = 0 - 200$  for simulation runs: (a) Run-1(I), (b) Run-1(VII), (c) Run-6(I), and (d) Run-6(VII). The dashed gray lines are from the linear dispersion of the IA waves which is derived by considering plasma quasi-neutrality approximation, whereas white dashed lines are from the dispersion relation of IA waves which is derived without consideration of the plasma quasi-neutrality approximation.

$\omega_{pi}t = 0 - 30$  for  $\kappa=2$  and  $20$  with different amplitude of IDP (a)  $\Delta n = 0.05$  and (b)  $\Delta n = 0.5$ . In case of all four simulation runs, both energies are zero at the equilibrium for  $\omega_{pi}t = 0$ . In each run, both potential and kinetic energies initially increase and attend the maximum value in the evolution of the finite electrostatic potential in the form of single pulse in the system. Later, the potential energy decreases

from the maximum. This decrease is due to the decrease in the amplitude of the potential pulse. As soon as the potential energy goes to its minimal, the corresponding electrostatic potential amplitude will stop decreasing further. This time is shown in the figure by the vertical dashed lines  $t_1$  for  $\kappa=20$  and  $t_2$  for  $\kappa=2$ . At these times, the trough is formed at the top point of the potential pulse, which breaks the pulse into

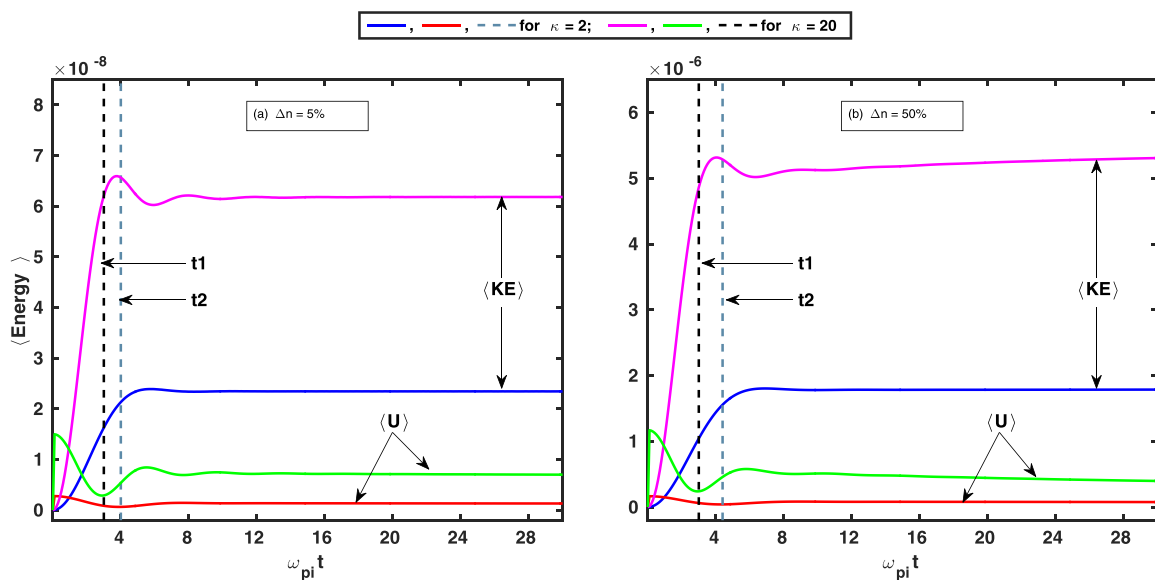


FIG. 4. The evolution of the average electrostatic energy  $\langle U \rangle$  and kinetic energy  $\langle KE \rangle$  of the ions in the system for the different kappa index and the amplitude of IDP for the runs discussed in Figure 2. The vertical dashed lines at time  $t_1$  (for  $\kappa=20$ ) and  $t_2$  (for  $\kappa=2$ ) show the time at which the trough formation begins at the top point of the potential pulse.

two identical solitary pulses. In the formation of two IASW pulses, the potential energy gradually increases, whereas the kinetic energy decreases. The major difference we observed is that the first minima of the potential energy comes early for  $\kappa = 20$  as compared with the simulation runs of  $\kappa = 2$ . Furthermore, both kinetic and potential energies remain constant after the formation of stable IA solitons. We also observed that the order of the potential and kinetic energies is higher (lower) for the higher (lower) amplitude of the IDP in the equilibrium densities. Similar trend is observed for the  $\kappa$  values. For large  $\kappa$  index, both energies have larger amplitudes in comparison with the small  $\kappa$  index.

To emphasize the contribution of the superthermal index  $\kappa$  in the formation of the IASW pulses, we have obtained the IASW pulse formation time for different simulation runs. In Figure 5, we have plotted the time at which the two IASW pulses formed in the system as a function of  $\kappa$  index for  $\Delta n = 0.05$  and  $0.5$ . From this figure, it is seen that the pulse formation time decreases with the increase of  $\kappa$  index for both IDPs. This decrease in time is considerably high for  $\kappa \leq 8$ , which then saturates for beyond  $\kappa > 8$ . Furthermore, it is seen that the formation of two IASW pulses occurs early in the system with smaller IDP than the system with larger IDP for fixed  $\kappa$  index.

#### IV. CHARACTERISTICS OF IA SOLITONS: THEORY VS SIMULATION

The nonlinear fluid theory of IA solitons uses the Sagdeev’s pseudopotential technique. This theory is used in many studies to model the ESWs in plasmas. Saini *et al.*<sup>35</sup> have used this approach to model the IA solitons for the plasma consisting of fluid ions and superthermal electrons. Equations (7)–(9) can be transformed to the stationary frame moving with the solitary wave speed  $V_s$ , i.e.,  $\xi = x_n - Mt_n$ , where  $M = V_s/C_{IA}$  is the Mach number with respect to the ion thermal velocity. Then, solving Equations (7) and (8) for perturbed density of ions and putting it in the Poisson equation, and assuming appropriate boundary conditions for the localized disturbances along with the conditions that  $\Phi = 0$ ,

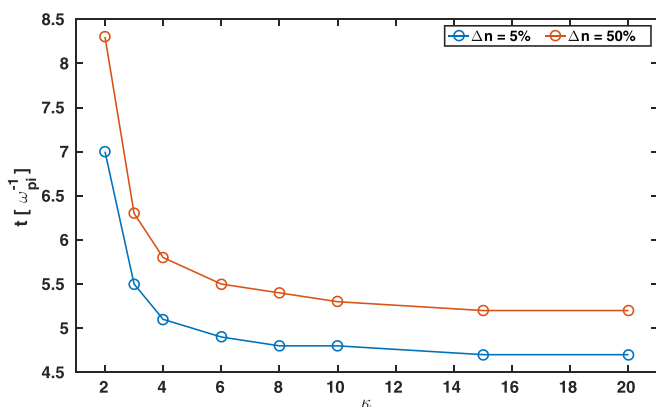


FIG. 5. The variation of the IASW pulse formation time (see Figure 2(c)) with the kappa index. The blue color is for the perturbation  $\Delta n = 0.05$  and the red color lines represent the case of the  $\Delta n = 0.5$  perturbation in ion and electron equilibrium densities.

and  $d\Phi/d\xi = 0$  at  $\xi \rightarrow \pm\infty$ , one can obtain the following energy integral<sup>35</sup>

$$\frac{1}{2} \left( \frac{d\Phi}{d\xi} \right)^2 + \psi(\Phi) = 0. \tag{16}$$

In the equation above,  $\psi(\Phi)$  is the pseudopotential, which is given as

$$\psi(\Phi) = M^2 \left[ 1 - \left( 1 - \frac{2\Phi}{M^2} \right)^{1/2} \right] + 1 - \left( 1 - \frac{\Phi}{\kappa - 3/2} \right)^{-\kappa+3/2}. \tag{17}$$

The lower limit of the Mach number  $M_{\min}$ , above which the solitary solutions exist is given as

$$M_{\min} = \left( \frac{\kappa - 3/2}{\kappa - 1/2} \right)^{1/2}. \tag{18}$$

The upper limit of Mach number  $M_{\max}$ , below which the solitary solutions exist is obtained by solving the following equation numerically

$$M_{\max}^2 + 1 - \left( 1 - \frac{M_{\max}^2}{2\kappa - 3} \right)^{-\kappa+3/2} = 0. \tag{19}$$

By using Equations (18) and (19), we have calculated the lower and upper Mach number range for the existence of IA solitons by varying the superthermal index  $\kappa$ , and it is shown with shaded region in Figure 6. Saini *et al.*<sup>35</sup> have also obtained the parametric range for the existence of the stationary solitary solution for the model considered here. We tried to validate the range of Mach numbers obtained from the nonlinear theory with our fluid simulations. Figure 6 shows the variation of the Mach numbers with respect to  $\kappa$  index. The asterisks with different colours in this figure correspond to the IA pulse speed obtained from the simulations

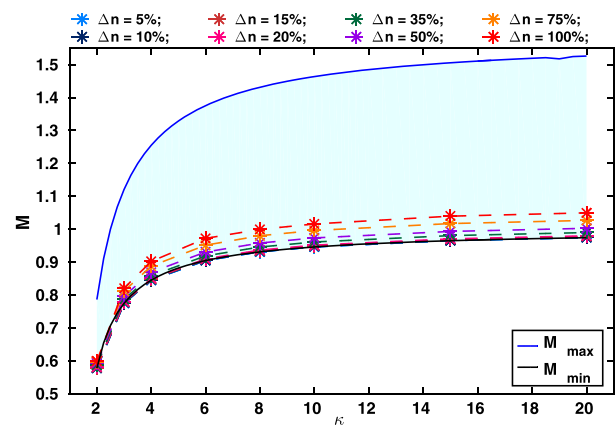


FIG. 6. Variation of Mach numbers with  $\kappa$ . The solid black line represents the lower ( $M_{\min}$ ) and the solid blue line represents the upper ( $M_{\max}$ ) Mach number limit predicted by nonlinear fluid theory for the existence of the IA solitons. Shaded region shows Mach number range for the existence domain of the IA solitons predicted by the nonlinear fluid theory. The different asterisk color points are the Mach numbers obtained from the simulation for different combinations of kappa and the amplitude of the IDP.

for different amplitude of the IDP. The speed of the IASW pulses is calculated in the region where these pulses are sufficiently stable. The stability region is chosen by observing the propagation of solitary pulse with nearly constant width and amplitude in the system. From Figure 6, it is observed that the Mach numbers associated with the lower amplitude IDPs are very close to the lower limit of the Mach number that is supported by the nonlinear fluid theory.

Our fluid simulation shows that the Mach number associated with the IA solitons increases with the increase of the amplitude of the IDP for the fixed value of the  $\kappa$  index. For the fixed amplitude of IDP, it is found that the speed of IA solitons quickly increases with the increasing of  $\kappa$  index up to 6. For  $\kappa > 6$ , the Mach numbers of the solitons are almost constant, which is in accordance with the nonlinear fluid theory. However, it is noticed that the speed of the IA solitons obtained from the simulation for  $\Delta n = 0.05 - 1$  is narrower than the range predicted by the nonlinear fluid theory.

We have also obtained the maximum amplitude and width of the stable IA solitons in the stability region from all simulation runs. These amplitudes and widths are verified with the amplitudes and widths obtained from the theory. To do so, we take the speed of IA pulse obtained from the simulation as an input to solve Equation (16) numerically. The numerical solution of this equation gives the profile of the  $\Phi$ , from which the corresponding amplitude and width of the IA soliton is calculated.

Figure 7 shows the variation of the maximum amplitude  $\Phi_{max}$  estimated from the theory and simulation with kappa index. The amplitude represented by asterisks in this figure is from the simulation data, while the circles represent the amplitudes obtained from the theory. This figure shows that the simulation results are in agreement with the results from the nonlinear fluid theory for  $\Delta n > 0.1$ . It is also observed that the maximum amplitude of the IA soliton increases with the increase of  $\kappa$  index. The increase in the amplitude after  $\kappa > 6$  is not significant, which is in agreement with the theory. The increase in the amplitude of the IDP increases the maximum amplitude of the solitons in the system for the fixed value  $\kappa$  index.

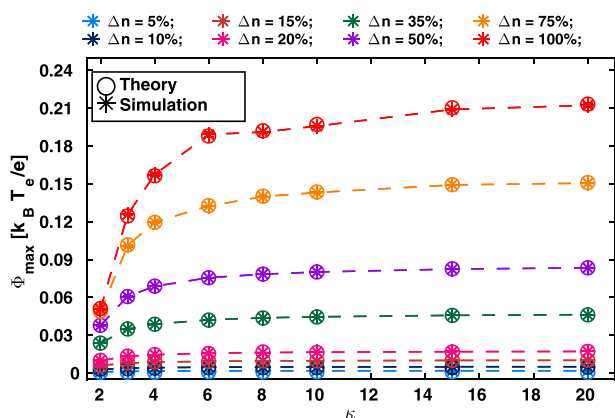


FIG. 7. Figure shows variation of the maximum electrostatic potential supported for different  $\kappa$  values and the different amplitude of the IDP. The circles represent the  $\Phi_{max}$  obtained from the theory, whereas the asterisks represent the  $\Phi_{max}$  obtained from simulation.

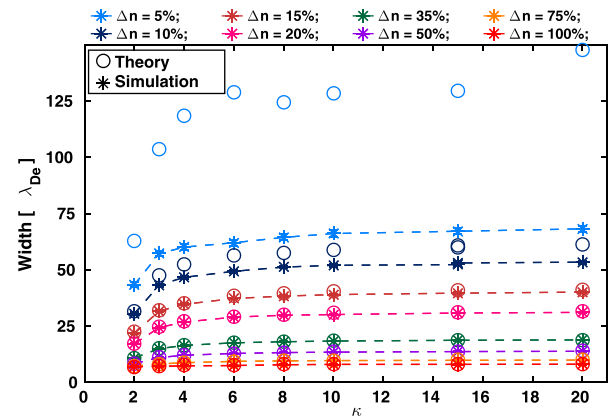


FIG. 8. Figure shows the variation of the maximum full width at half maximum for different combinations of the  $\kappa$  and IDP amplitude. The circles represent the  $\Phi_{max}$  obtained from the theory, whereas the asterisks represent the soliton widths obtained from the simulation.

Figure 8 shows the variation of the width of the IA solitons with the kappa index from the theory and simulation. The points represented by the asterisks in this figure are from the simulation data and the circles are from the theory. In this case, the simulation results are well matching with the theoretical results for the IDPs with amplitude  $\Delta n > 0.1$ . This figure shows that the widths of the solitons increase with the increase of the  $\kappa$  index. For any fixed  $\kappa$  index, the widths are larger for lower amplitude IDPs, whereas for large amplitude IDPs, the soliton widths are smaller. In all simulation runs, the soliton widths beyond  $\kappa = 6$  are nearly the same.

For the lower amplitude perturbations ( $\Delta n \leq 0.1$ ), there are differences in the amplitudes ( $\Phi_{max}$ ) and width of IA pulse obtained from the theory and simulation. It should be noted that nonlinear theory gives the information about stable solutions supported by the plasma system. The present fluid simulation shows that apart from stable IA pulses, the IA oscillations are also present in the plasma system. When the amplitude of IDP is smaller ( $\Delta n \leq 0.1$ ), the IA oscillations and IA pulse are found to be moving with nearly same speed. Hence, the IA oscillations in these cases did not detach from the IA pulse. The near presence of dispersive IA oscillations affects the characteristics like width and amplitude of the IA pulse. Thus, for lower amplitude perturbations ( $\Delta n \leq 0.1$ ), there is disagreement in the characteristics of IA pulse obtained from simulation and theory. It suggests that the solitary solutions obtained from the nonlinear fluid theory for the Mach numbers very close to the lower limit of the Mach number range, i.e.,  $M_{min}$  is not appropriate to model the ESWs supported by the plasma system.

### V. CONCLUSIONS

In this paper, we have studied the evolution and propagation of the IA waves in a plasma composed of cold fluid ions and superthermal electrons following the kappa velocity distribution function. To the best of our knowledge, this is the first simulation that includes electrons following nonthermal kappa velocity distribution, which is often observed in space plasmas.

We found that the IDP introduced in the plasma system evolves into two indistinguishable sets of IA oscillations and IASW pulses. The IA oscillations follow the IASW pulses such that  $V_{s0} \leq M_{\min} < V_s$ . The IA oscillations are found to be dispersive mode that propagates in a system with constant ion plasma frequency, whereas the IASW pulses are found to be nondispersive and they propagate in the system with constant speed. The simulation runs performed by varying the amplitude of the IDP indicates that the IDP evolves into the strong dispersive IA waves along with very weak nondispersive IA waves, when the IDP amplitude  $\Delta n < 0.1$ . On the other hand, when the amplitude of IDP is above 10%, strong dispersive and nondispersive IA waves are generated in the system.

From the spatio-temporal evolution analysis, we conclude that the decrease in the population of superthermal electrons (i.e., higher  $\kappa$  index) generates more dispersive IA oscillations than the system with lower  $\kappa$  index. The IA oscillations become more dispersive and cover wider spatial extent for the higher amplitude IDPs and the superthermal kappa index. The fluid simulation shows that the IDP with higher (smaller) amplitude generates large (small) amplitude IASWs in the system. It is concluded that the increase of superthermal index increases the speeds of the IA oscillations and IASWs, for the fixed amplitude of the IDP in the system. In case of the fixed superthermal index, as the amplitude of the IDP increases the speed of the IA oscillations and IASWs increased. It is seen that the time required for the formation of IA mode is lesser for higher kappa index. It suggests that the IASWs are generated faster in the plasma that follows the thermal distribution. From the estimation of the average kinetic and potential energies during evolution of the IASWs, it is observed that the energies remain constant when the nonlinearity and the dispersion in the system get balanced. Furthermore, it is found that the formation of IA solitons evolved earlier for the simulation runs with large kappa index and the IDP with large amplitude.

It is observed that the IA pulses become significantly stable during the course of their propagation and their characteristics like width, amplitude ( $\Phi_{\max}$ ), and speed ( $V_s$ ) are nearly constant in this stability region. The IA soliton characteristics obtained from the fluid theory and simulations are compared. The existence of the two identical IA solitons moving in opposite directions with the constant speed is predicted by the nonlinear fluid theory, which is consistent with the simulation results. It is observed that the Mach numbers of the IA solitons obtained from the simulation for different amplitude of the IDP are found to be in the existence region predicted by the nonlinear fluid theory. However, our simulation suggests that the IA soliton characteristics obtained from the nonlinear fluid theory closer to the lower limit of Mach number range (i.e.,  $M_{\min}$ ) are not appropriate. For the fixed width of the perturbation, the maximum Mach number predicted by the nonlinear theory is not achievable with the IDP with 100% amplitude. In reality, it is not possible to have the 100% perturbation. These observations manifest the overestimation of the existence limit given by the nonlinear theory.

## ACKNOWLEDGMENTS

The model computations were performed on the High Performance Computing System at the Indian Institute of Geomagnetism. Authors are grateful to Professor D. S. Ramesh, Director, Indian Institute of Geomagnetism (IIG), for his encouragement and support in establishing new high performance computing facility at IIG.

- <sup>1</sup>L. Wilson III, C. Cattell, P. Kellogg, K. Goetz, K. Kersten, L. Hanson, R. MacGregor, and J. Kasper, "Waves in interplanetary shocks: A wind/waves study," *Phys. Rev. Lett.* **99**, 041101 (2007).
- <sup>2</sup>F. Mozer, S. Bale, J. Bonnell, C. Chaston, I. Roth, and J. Wygant, "Megavolt parallel potentials arising from double-layer streams in the earth's outer radiation belt," *Phys. Rev. Lett.* **111**, 235002 (2013).
- <sup>3</sup>F. Mozer, O. Agapitov, A. Artemyev, J. Burch, R. Ergun, B. Giles, D. Mourenas, R. Torbert, T. Phan, and I. Vasko, "Magnetospheric multiscale satellite observations of parallel electron acceleration in magnetic field reconnection by Fermi reflection from time domain structures," *Phys. Rev. Lett.* **116**, 145101 (2016).
- <sup>4</sup>B. Lefebvre, L.-J. Chen, W. Gekelman, P. Kintner, J. Pickett, P. Pribyl, and S. Vincena, "Debye-scale solitary structures measured in a beam-plasma laboratory experiment," *Nonlinear Processes Geophys.* **18**, 41–47 (2011).
- <sup>5</sup>J. S. Pickett, L.-J. Chen, O. Santolík, S. Grimald, B. Lavraud, O. P. Verkhoglyadova, B. T. Tsurutani, B. Lefebvre, A. Fazakerley, G. S. Lakhina, S. S. Ghosh, B. Grison, P. M. E. Décréau, D. A. Gurnett, R. Torbert, N. Cornilleau-Wehrin, I. Dandouras, and E. Lucek, "Electrostatic solitary waves in current layers: From cluster observations during a super-substorm to beam experiments at the LAPD," *Nonlinear Processes Geophys.* **16**, 431–442 (2009).
- <sup>6</sup>H. Matsumoto, H. Kojima, T. Miyatake, Y. Omura, M. Okada, I. Nagano, and M. Tsutsui, "Electrostatic solitary waves (ESW) in the magnetotail: BEN wave forms observed by GEOTAIL," *Geophys. Res. Lett.* **21**, 2915–2918, doi:10.1029/94GL01284 (1994).
- <sup>7</sup>J. R. Franz, P. M. Kintner, and J. S. Pickett, "Polar observations of coherent electric field structures," *Geophys. Res. Lett.* **25**, 1277–1280, doi:10.1029/98GL50870 (1998).
- <sup>8</sup>F. Mottez, "Instabilities and formation of coherent structures," in *Physics of Space: Growth Points and Problems* (Springer, 2001), pp. 59–70.
- <sup>9</sup>H. Washimi and T. Taniuti, "Propagation of ion-acoustic solitary waves of small amplitude," *Phys. Rev. Lett.* **17**, 996 (1966).
- <sup>10</sup>N. Dubouloz, R. Treumann, R. Pottelette, and M. Malingre, "Turbulence generated by a gas of electron acoustic solitons," *J. Geophys. Res.: Space Phys.* **98**, 17415–17422, doi:10.1029/93JA01611 (1993).
- <sup>11</sup>A. Kakad, S. Singh, R. Reddy, G. Lakhina, and S. Tagare, "Electron acoustic solitary waves in the earth's magnetotail region," *Adv. Space Res.* **43**, 1945–1949 (2009).
- <sup>12</sup>N. J. Zabusky and M. D. Kruskal, "Interaction of "solitons" in a collisionless plasma and the recurrence of initial states," *Phys. Rev. Lett.* **15**, 240 (1965).
- <sup>13</sup>C. S. Gardner, J. M. Greene, M. D. Kruskal, and R. M. Miura, "Method for solving the Korteweg-deVries equation," *Phys. Rev. Lett.* **19**, 1095 (1967).
- <sup>14</sup>N. Singh, "High-Mach number electrostatic shocks in collisionless plasmas," *Indian Institute of Technology, Kanpur*, **11**(7), 533–534 (1973).
- <sup>15</sup>M. Berthomier, R. Pottelette, and M. Malingre, "Solitary waves and weak double layers in a two-electron temperature auroral plasma," *J. Geophys. Res.: Space Phys.* **103**, 4261–4270, doi:10.1029/97JA00338 (1998).
- <sup>16</sup>R. Sagdeev, "Cooperative phenomena and shock waves in collisionless plasmas," *Rev. Plasma Phys.* **4**, 23 (1966).
- <sup>17</sup>A. Kakad, S. Singh, R. Reddy, G. Lakhina, S. Tagare, and F. Verheest, "Generation mechanism for electron acoustic solitary waves," *Phys. Plasmas* **14**, 052305 (2007).
- <sup>18</sup>G. Lakhina, A. Kakad, S. Singh, and F. Verheest, "Ion-and electron-acoustic solitons in two-electron temperature space plasmas," *Phys. Plasmas* **15**, 062903 (2008).
- <sup>19</sup>T. K. Baluku, M. A. Hellberg, and F. Verheest, "New light on ion acoustic solitary waves in a plasma with two-temperature electrons," *Europhys. Lett.* **91**, 15001 (2010).

- <sup>20</sup>F. Verheest, M. A. Hellberg, and I. Kourakis, "Ion-acoustic supersolitons in plasmas with two-temperature electrons: Boltzmann and kappa distributions," *Phys. Plasmas* **20**, 082309 (2013).
- <sup>21</sup>S. Bame, J. Asbridge, H. Felthuser, E. Hones, and I. Strong, "Characteristics of the plasma sheet in the earth's magnetotail," *J. Geophys. Res.* **72**, 113–129, doi:10.1029/JZ072i001p00113 (1967).
- <sup>22</sup>S. Christon, "A comparison of the mercury and earth magnetospheres: Electron measurements and substorm time scales," *Icarus* **71**, 448–471 (1987).
- <sup>23</sup>C. Kletzing, J. Scudder, E. Dors, and C. Curto, "Auroral source region: Plasma properties of the high-latitude plasma sheet," *J. Geophys. Res.: Space Phys.* **108**(A10), 1360, doi:10.1029/2002JA009678 (2003).
- <sup>24</sup>V. Formisano, P. Hedgecock, G. Moreno, F. Palmiotto, and J. Chao, "Solar wind interaction with the earth's magnetic field: 2. Magnetohydrodynamic bow shock," *J. Geophys. Res.* **78**, 3731–3744, doi:10.1029/JA078i019p03731 (1973).
- <sup>25</sup>V. Pierrard and J. Lemaire, "Fitting the AE-8 energy spectra with two Maxwellian functions," *Radiat. Meas.* **26**, 333–337 (1996).
- <sup>26</sup>F. Xiao, C. Shen, Y. Wang, H. Zheng, and S. Wang, "Energetic electron distributions fitted with a relativistic kappa-type function at geosynchronous orbit," *J. Geophys. Res.: Space Phys.* **113**(A05), 203, doi:10.1029/2007JA012903 (2008).
- <sup>27</sup>G. Gloeckler, J. Geiss, H. Balsiger, P. Bedini, J. Cain, J. Fischer, L. Fisk, A. Galvin, F. Gliem, D. Hamilton *et al.*, "The solar wind ion composition spectrometer," *Astron. Astrophys. Suppl. Ser.* **92**, 267–289 (1992).
- <sup>28</sup>M. Maksimovic, V. Pierrard, and P. Riley, "Ulysses electron distributions fitted with kappa functions," *Geophys. Res. Lett.* **24**, 1151–1154, doi:10.1029/97GL00992 (1997).
- <sup>29</sup>H. Ikezi, R. Taylor, and D. Baker, "Formation and interaction of ion-acoustic solitons," *Phys. Rev. Lett.* **25**, 11 (1970).
- <sup>30</sup>Y. Nakamura and A. Sarma, "Observation of ion-acoustic solitary waves in a dusty plasma," *Phys. Plasmas* **8**, 3921–3926 (2001).
- <sup>31</sup>S. Olbert, "Summary of experimental results from MIT detector on IMP-1," in *Physics of the Magnetosphere* (Springer, 1968), pp. 641–659.
- <sup>32</sup>V. M. Vasyliunas, "A survey of low-energy electrons in the evening sector of the magnetosphere with OGO 1 and OGO 3," *J. Geophys. Res.* **73**, 2839–2884, doi:10.1029/JA073i009p02839 (1968).
- <sup>33</sup>D. Summers and R. M. Thorne, "The modified plasma dispersion function," *Phys. Fluids B* **3**, 1835–1847 (1991).
- <sup>34</sup>V. Pierrard and M. Lazar, "Kappa distributions: Theory and applications in space plasmas," *Sol. Phys.* **267**, 153–174 (2010).
- <sup>35</sup>N. Saini, I. Kourakis, and M. Hellberg, "Arbitrary amplitude ion-acoustic solitary excitations in the presence of excess superthermal electrons," *Phys. Plasmas* **16**, 062903 (2009).
- <sup>36</sup>N. Saini and I. Kourakis, "Electron beam-plasma interaction and ion-acoustic solitary waves in plasmas with a superthermal electron component," *Plasma Phys. Controlled Fusion* **52**, 075009 (2010).
- <sup>37</sup>G. Lakhina and S. Singh, "Generation of weak double layers and low-frequency electrostatic waves in the solar wind," *Sol. Phys.* **290**, 3033–3049 (2015).
- <sup>38</sup>T. Baluku and M. Hellberg, "Dust acoustic solitons in plasmas with kappa-distributed electrons and/or ions," *Phys. Plasmas* **15**, 123705 (2008).
- <sup>39</sup>T. Baluku, M. Hellberg, I. Kourakis, and N. Saini, "Dust ion acoustic solitons in a plasma with kappa-distributed electrons," *Phys. Plasmas* **17**, 053702 (2010).
- <sup>40</sup>T. Baluku and M. Hellberg, "Ion acoustic solitons in a plasma with two-temperature kappa-distributed electrons," *Phys. Plasmas* **19**, 012106 (2012).
- <sup>41</sup>A. Kakad, Y. Omura, and B. Kakad, "Experimental evidence of ion acoustic soliton chain formation and validation of nonlinear fluid theory," *Phys. Plasmas* **20**, 062103 (2013).
- <sup>42</sup>B. Kakad, A. Kakad, and Y. Omura, "Nonlinear evolution of ion acoustic solitary waves in space plasmas: Fluid and particle-in-cell simulations," *J. Geophys. Res.: Space Phys.* **119**, 5589–5599, doi:10.1002/2014JA019798 (2014).
- <sup>43</sup>A. Kakad, B. Kakad, C. Anekallu, G. Lakhina, Y. Omura, and A. Fazakerley, "Slow electrostatic solitary waves in earth's plasma sheet boundary layer," *J. Geophys. Res.: Space Phys.* **121**, 4452–4465, doi:10.1002/2016JA022365 (2016).
- <sup>44</sup>K. Watanabe and T. Sato, "High-precision MHD simulation," in *Computer Space Plasma Physics: Simulation Techniques and Software* (Terra Scientific, Tokyo, Japan, 1993), pp. 209–215.
- <sup>45</sup>Y. Omura and J. L. Green, "Plasma wave signatures in the magnetotail reconnection region: MHD simulation and ray tracing," *J. Geophys. Res.: Space Phys.* **98**, 9189–9199, doi:10.1029/92JA02901 (1993).
- <sup>46</sup>A. Lotekar, A. Kakad, and B. Kakad, "Stability and convergence of Poisson solver in a fluid plasma simulation with velocity distribution functions," *Comput. Phys. Commun.* (unpublished).